ARTICLE   OPEN

From hidden metal-insulator transition to Planckian-like dissipation by tuning the oxygen content in a nickelate

Qikai Guo [1] and Beatriz Noheda [1,2 ✉]

Heavily oxygen-deficient NdNiO$_3$ (NNO) films, which are insulating due to electron localization, contain pristine regions that undergo a hidden metal-insulator transition. Increasing oxygen content increases the connectivity of the metallic regions and the metal-insulator transition is first revealed, upon reaching the percolation threshold, by the presence of hysteresis. Only upon further oxygenation is the global metallic state (with a change in the resistivity slope) eventually achieved. It is shown that sufficient oxygenation leads to linear temperature dependence of resistivity in the metallic state, with a scattering rate directly proportional to temperature. Despite the known difficulties to establish the proportionality constant, the experiments are consistent with a relationship $1/\tau = \alpha k_B T/\hbar$, with α not far from unity. These results could provide experimental support for recent theoretical predictions of disorder in a two-fluid model as a possible origin of Planckian dissipation.

INTRODUCTION

Among the perovskites, the rare-earth nickelates (RENiO$_3$) are interesting because of their tunable metal-insulator transition (MIT)[1–8]. Recent seminal works directly imaging the evolution of metal and insulating regions, have greatly contributed to a better understanding of the phase transition in these materials[9–13] but important questions remain, such as why are the metallic regions still present at low temperatures[9] or what is the origin of the critical behavior observed at the (first-order) phase transition[12]. RENiO$_3$ are also attracting renewed attention due to the discovery of a superconducting phase in the family of the infinite-layer nickelates[14,15], which are an oxygen-deficient version of the perovskite nickelates, obtained by removal of a full layer of oxygen atoms. However, most often, oxygen vacancies (V_o) in nickelates are randomly distributed through the lattice, with a different effect on the transport properties[16–20]. In particular, these randomly distributed V_o are known to give rise to electron localization in defect states[16,17,19,21].

In addition, NNO films have been reported to show bad metal behavior[22], characterized by exceedingly short electron relaxation times; while in other strongly correlated materials, such as cuprate superconductors or heavy fermions, strange metal behavior and Planckian dissipation is observed[23,24]. This is a recent concept put forward to explain low temperature resistivity that is independent of the strength of the electron interactions and scales linearly with temperature[25,26], defying expected quadratic Fermi liquid behavior. However, in NNO, linear behavior of the resistivity has only been rarely claimed[27,28]. In NNO thin films, other scaling exponent ($1 \leq n < 2$) have also been reported[29–34], which are proposed to arise from spin fluctuations, due to the proximity to a quantum critical point, and to vary with strain[29,30]. In addition, it has also been shown, in nickelates and in other electron correlated materials, that the apparent exponents experimentally obtained, strongly depend on the quenched disorder induced, for example, by the presence of V_o[35–37].

These findings emphasize the importance of controlling V_o in RENiO$_3$. In this work, we present a study on the effect of the oxygen content in a NdNiO$_3$ (NNO) film grown on an YAlO$_3$ (YAO) substrate under highly-compressive strain conditions, which allows us to decouple the effects of strain and disorder. Appropriate analysis of the evolution of the resistivity (ρ) versus temperature (T) curves with oxygen content offers a clear picture of the microscopic mechanisms at play, supporting the recent idea that Planckian metal behavior can arise from a two-fluid scenario in a disorder Hubbard model[38].

RESULTS

Hidden metal-insulator transition

Epitaxial NdNiO$_3$ (NNO) films are grown on YAlO$_3$ (YAO) substrates by pulsed laser deposition (see Methods). A 20 nm thick NNO film is subjected to high vacuum conditions right after growth, in order to produce a large amount of V_o (see a sketch in Supplementary Fig. 1a). Supplementary Figures 1b, c show, respectively, the atomic force microscopy (AFM) image of the film topography and the X-ray diffraction patterns, attesting the atomically flat, single-crystalline, epitaxial, (001)-oriented nature of the film. Then, the oxygen content is gradually increased by subjecting the same film to increasingly higher annealing temperatures (T_a) in an oxygen atmosphere. As shown in Supplementary Fig. 1c, the (002)-diffraction peak shows a shift towards increasing angles, corresponding to a reduction in the out-of-plane lattice parameter and manifesting the decrease of V_o content (see an estimation in the Supplementary Information) in the film[16,17].

Figure 1 a shows the ρ-T curves of the NNO/YAO film measured after different annealing stages, giving rise to various oxygen content levels. The ρ-T dependence of the film annealed either in vacuum or in oxygen at a low T_a, shows semiconducting behavior, as expected for a film with a large amount of defects[19]. In order to observe a clear change in the sign of the resistivity derivative, a T_a of 800 °C in an oxygen-enriched environment is needed. Under these conditions the film shows a clear metal-to-insulator transition temperature (T_{MI}) at 170 K (see Supplementary Fig. 2). For intermediate states, a progressive decrease of ρ is observed

[1]Zernike Institute for Advanced Materials, University of Groningen, Groningen, The Netherlands. [2]CogniGron (Cognitive Systems and Materials Center), University of Groningen, Groningen, The Netherlands. ✉email: b.noheda@rug.nl
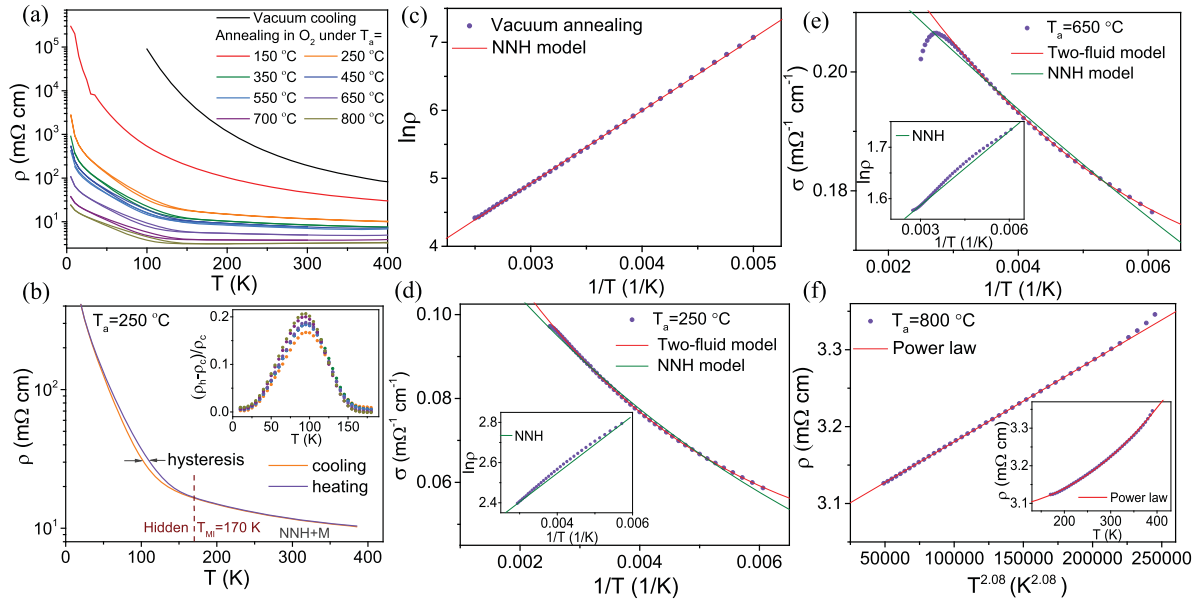
Fig. 1 Modulation of conduction by disorder. a Temperature (T) dependence of resistivity (ρ) (ρ-T) during cooling and heating for the same 20 nm thick NNO thin film grown on an YAO substrate, after annealing at increasingly larger temperatures. **b** ρ-T measurements during heating (ρ_h) and cooling (ρ_c), after annealing at $T_a = 250\,°C$. The inset shows the difference between the heating and cooling curves in **a**. **c** Ln (ρ)-$1/T$ measured in the NNO/YAO film annealed in vacuum, together with the fit to a NNH model for $T \geq 170\,K$. After annealing at $T_a = 250\,°C$ **d** and 650 °C **e**, the conductivity (σ) versus T fits best to the two-fluid model of Eq. (2) ($n = 1$). The insets in **d** and **e** plotting ln ρ-$1/T$, highlight the inadequacy of a NNH fitting model. **f** The same NNO/YAO film after annealing at 800 °C for 1 h displays a metal-like ρ-T (inset) with a scaling exponent $n = 2.08$.

under increasingly T_a, in agreement with a systematic reduction in the amount of V_o in the film. However, the temperature dependence of ρ remains insulator-like for T_a up to 700 °C.

In spite of the absence of a change in the temperature derivative of the resistivity, the existence of thermal hysteresis below 170 K, as shown in Fig. 1b and Supplementary Fig. 2a, for T_a above 250 °C, is consistent with the coexistence of metallic and insulating regions in an extended temperature range down to 20 K and it is a clear manifestation of the existence of the metal-insulator transition, as expected in pristine NNO[10]. In the following, we describe how the metallic regions contribute to the resistivity.

Change of conduction mechanism by modulating disorder

As shown in Fig. 1c and Supplementary Figs. 3 and 4, the ρ-T curves of the sample cooled down from the growth in vacuum, as well as after annealing in O_2 at 150 °C (with the largest and second largest amount of V_o), follow a Nearest Neighbors Hopping (NNH) model for $T \geq 170\,K$. The NNH conduction model is commonly employed in semiconducting systems[39,40] and is described by a simple activation process:

$$\rho(T) = \rho_0 \exp(E_a/k_B T) \qquad (1)$$

where the ρ_0 is a prefactor, E_a is the thermal activation energy of hopping electrons, and k_B is the Boltzmann constant. This model, however, does not apply to the same sample with higher oxygen contents (250 °C $\leq T_a \leq$ 650 °C), as seen from the worsening of the NNH fit in Fig. 1d, e and Supplementary Fig. 3b. Under these conditions, the film shows hysteresis in the ρ-T curve, as a clear indication of the metal-insulator transition and, thus, of the presence of metallic patches in the samples. The metallic regions are expected to change the resistivity behavior, which deviates from the NNH model. Indeed, the data are shown to follow a two-fluid NNH+M model[35,41,42] that describes the combined contribution of semiconducting regions, with localized electrons (NNH)

and metallic regions, with itinerant electrons (M). The total ρ is then trivially calculated by the parallel combination of these two components as:

$$\frac{1}{\rho(T)} = \frac{1}{\rho_0^* \exp(E_a/k_B T)} + \frac{1}{\rho^*(0) + A^* T^n} \qquad (2)$$

where ρ_0^* is the prefactor of the NNH contribution, normalized by geometrical factors describing the regions of defective insulating phase, while A^* measures the electron interactions in the metallic regions, normalized by a geometrical factors associated to the pristine metallic phase and $\rho^*(0)$ is the residual resistivity. For convenience, conductivity (σ) rather than ρ was used in the fitting (see Fig. 1d, e and Supplementary Fig. 4). This parallel arrangement implies that the O–Ni–O bonds in the metallic patches form a connected network in the volume between the electrodes, forming a metallic path through the sample (reaching the percolation threshold).

It can also be observed (see inset of Fig. 1b) that both the local T_{MI} and the thermal hysteresis ($\Delta T = 170–20\,K$) remain unchanged during oxygenation, thus, displaying no size dependence as the metallic percolated regions grow in size through the material. This shows that the material of the initial percolating metallic path has the same composition (oxygen content) as the subsequently formed paths, strongly indicating that the metallic regions are made of pristine $NdNiO_3$. Altogether, the data shows that metallic conduction at $T \geq T_{MI}$ takes place as the stoichiometric regions percolate through the sample, even if the material does not show metallic-like overall behavior due to the presence of a too large number of V_o. The E_a values extracted from the fits are plotted as a function of T_a in Supplementary Fig. 5. We will discuss these values in the next section.

After annealing at 800 °C in a oxygen-rich atmosphere, a robust metallic behavior of ρ is obtained in the formerly oxygen-deficient NNO film (see Fig. 1f). However, the film is not fully oxygenated yet, the V_o content can decrease further by increasing the

(a)

(b)

Annealing time at 800 °C (h)

Tensile strain

Compressive strain

Nearly strain-free
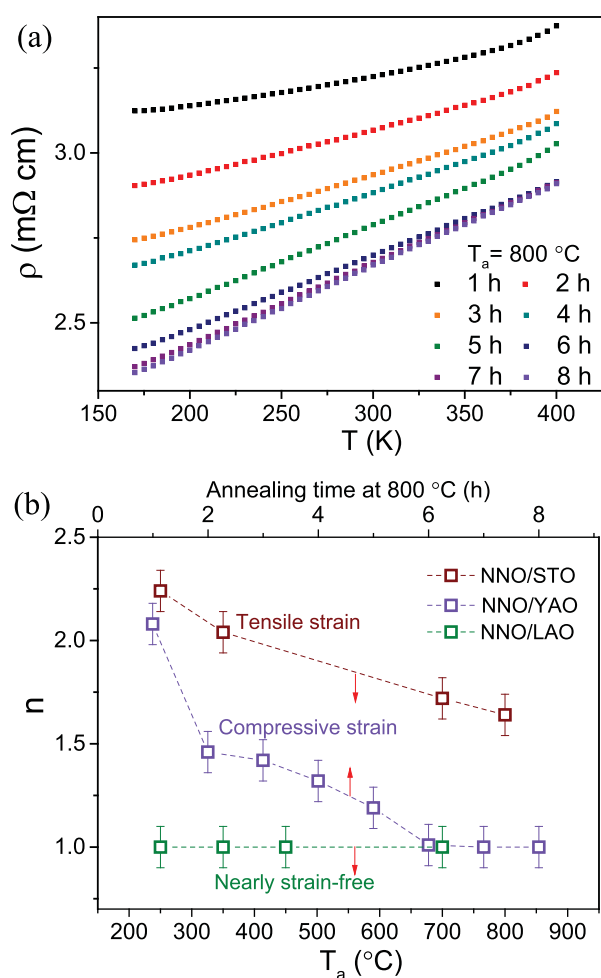
Fig. 2 Tunable resistivity scaling by regulating disorder. a Resistivity of NNO/YAO film as a function of temperature after annealing in an oxygen-enriched environment at 800 °C with various annealing times. **b** Evolution of exponents n with the annealing process in 20 nm NNO films grown on three different substrates. Data of NNO/LAO and NNO/STO were extracted from previous work[37]. In **b**, error bars are obtained from the fitted model described in the main text.

annealing time, which is demonstrated by the progressive decrease of resistivity shown in Fig. 2a.

As usual, ρ-T in the metallic NNO state can be well fit with a power law added to the residual resistivity (ρ - $\rho(0) \propto AT^n$). The evolution of the extracted values of n (see Supplementary Fig. 6 for the method of extraction) is plotted in Fig. 2b and shows a gradual decrease with decreasing disorder, reaching $n = 1$ for sufficiently low vacancy content. The results of similar experiments performed in NNO films under tensile strain (on SrTiO₃) and in quasi-strain-free films (on LaAlO₃)[37] are also plotted in the same figure for comparison.

A direct characterization of the conduction inhomogeneity in oxygen-deficient NNO/YAO films was obtained by using conductive atomic force microscopy (c-AFM). During the scanning, a direct-current sample bias was applied between the tip and the sample (see a sketch in the inset of Fig. 3a and a detailed explanation in the Methods). The sample after annealing at 800 °C for 1 h, displays two distinctly different types of regions, as shown in Fig. 3a. Comparison between Fig. 3a and the height map of the same area (see Supplementary Fig. 7) reveals that the observed contrast is not due to topographic features. I-V measurements were performed in two representative points (1 and 2) of Fig. 3a.

Notably, the current of point 1 shows a clear linear dependence with the applied voltage, indicating a robust metallic behavior in this local area (Fig. 3b). On the contrary, the current of point 2 only displays a slight voltage dependence and with much smaller current values than those of point 1 (Fig. 3c).

A comparable measurement was also performed in the heavily oxygen-deficient NNO/YAO sample (after vacuum annealing). As shown in Fig. 3d, the heavily oxygen-deficient NNO/YAO sample also presents inhomogeneous conduction. However, a voltage of 1.0 V, significantly larger than that applied to the 800 °C annealed sample (500 mV), is needed, indicating a less conducting behavior due to a higher oxygen-deficiency. A more pronounced difference of these two states was revealed by the I-V measurements. While the current of the NNO/YAO sample after annealing at 800 °C shows a robust linear-dependence with voltage, the NNO/YAO sample after vacuum annealing displays a clear semiconductor-like performance (see Fig. 3e, f), manifesting a distinct conduction mechanism in these two states. All of these results are well consistent with our hypothesis discussed above.

DISCUSSION
Our results are consistent with a description of oxygenation giving rise to a percolation process (see a sketch in Fig. 4). In the initial state, the NNO film after vacuum cooling possesses a large amount of Ni²⁺, acting as a semiconducting matrix (gray regions in Fig. 4). The ρ-T then follows a NNH model for $T > 170$ K (which is the T_{MI} of the nearly-stoichiometric film), while a Variable Range Hopping (VRH) mechanism is found to dominate in the lower temperature range (see Supplementary Fig. 8), indicating a change in hopping behavior as a precursor of the metal-insulator transition, even if no metallic behavior is yet observed. For $T_a = 250$ °C, the first percolation paths of stoichiometric regions form across the film. Above T_{MI}, these paths are metallic but, as they are surrounded by the dominant insulating (defective) matrix, the film still shows semiconductor character ($d\rho(T)/dT < 0$). Indeed, an excellent fit to the data is presented by an NNH+M two-fluid model, which includes itinerant electron metallic resistance in parallel with the resistance contributed by regions that host localized hopping electrons, for all intermediate $T_a = 250$–650 °C (see Fig. 1d, e and Supplementary Fig. 4). For each stage of annealing, and upon decreasing the environment temperature, the stoichiometric percolation paths undergo a metal-insulator transition, which is visible as a thermal hysteresis below the local T_{MI} (marked by green solid lines in Fig. 4). For sufficiently long annealing at 800 °C, the metallic regions cover large enough volume ratio to show a sign change in the ρ-T slope (($d\rho(T)/dT > 0$)). This is in agreement with previous reports of NNO films grown on YAO substrates showing a robust metallic ρ-T dependence[29,30,43].

The progressive oxygenation of the non-stoichiometric matrix is accompanied by local transformations of different types of polyhedra. In nickelates, oxygen-deficiency usually leads to a square pyramidal NiO₅ coordination. However, in heavily deficient cases, NiO₄ with either tetrahedral or square-planar configurations can also be formed if two oxygen atoms of the same octahedron are removed[19]. With increase of oxygen content, the transformation from NiO₄ to NiO₅ coordination could be expected. This change in the type of polyhedra could be the reason for the observed change in E_a with T_a in the first two states (see Supplementary Fig. 5), different from the constant value of E_a in the intermediate annealing states. $E_a \simeq 20$ meV is consistent with those reported in the normal semiconducting phases of nickelates[44–47]. However, a clear evolution of the A^*-coefficients with decreasing V_o is observed in the intermediate states, indicating a progressive increase of the volume fraction of metallic regions, as expected.
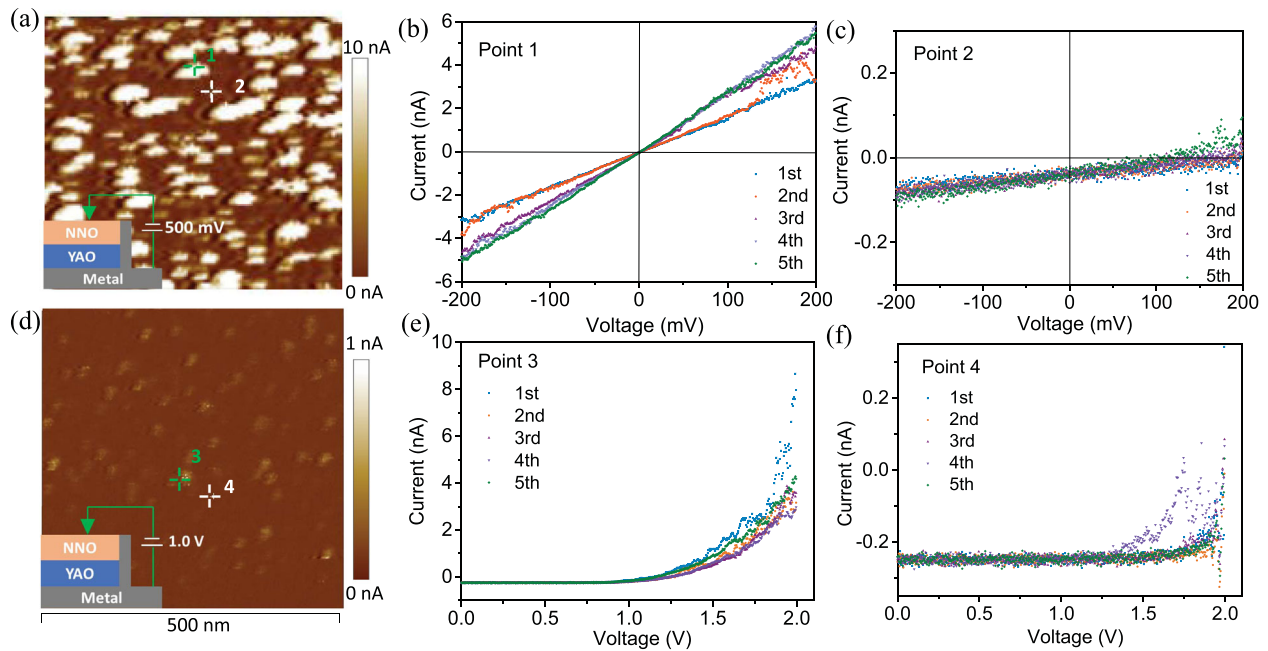
Fig. 3   Conductive Atomic force microscopy (c-AFM). a c-AFM image of the NNO/YAO film after annealing at 800° for 1 h with a DC sample bias of 500 mV. The inset sketch illustrates the configuration of the c-AFM measurement. **b, c** show the *I-V* curves obtained from representative points 1 and 2 in **a**, respectively. **d** c-AFM image of the NNO/YAO film after vacuum annealing with a DC sample bias of 1.0 V. **e, f** show the *I-V* curves obtained from representative point 3 and 4 in **d**, respectively.
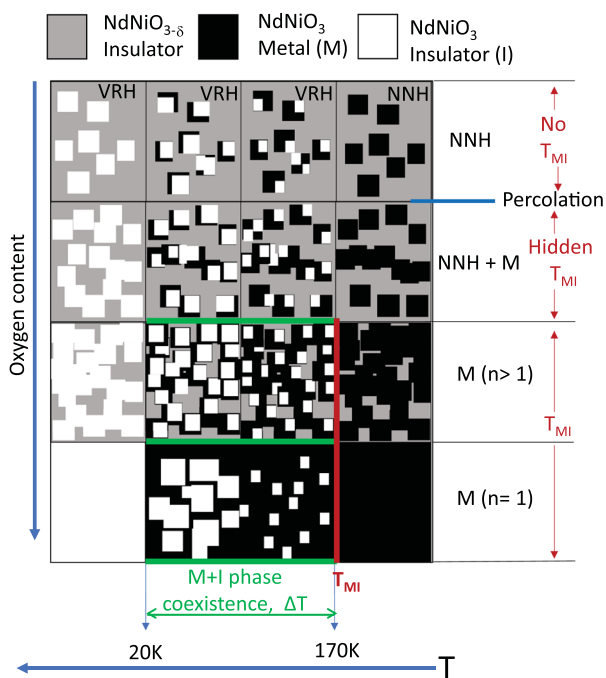
Fig. 4   Illustration of the double percolation model. The sketch shows the evolution of NNO films as a function of oxygen content (vertical) and temperature (horizontal). Gray, black and white denote electron-localized (defective) $NdNiO_{3-\delta}$, metallic $NdNiO_3$ and insulating $NdNiO_3$, respectively. The evolution of conduction models as a function of oxygen content (from NNH to NNH+M to M) are denoted. The blue horizontal line signifies the metallic percolation threshold. The green horizontal lines indicate the extent of the hysteresis (coexistence of M and I), while the red vertical line points out the measurable T_{MI}.

While the metal-insulator transition is clearly of first-order, the order of the percolation transition under oxygenation still needs investigation. A second-order percolation transition, as in VO_2[48], could offer an alternative explanation for the fractal antiferromagnetic structures observed in ref. [12]. This could perhaps also explain the coexistence of first-order and second-order features also reported in these materials[11].

Finally, we discuss the temperature scaling of ρ in the recovered metallic state of annealed NNO films on YAO (under compressive strain) in Fig. 2b. In the same figure, we add the NNO films on STO substrates (NNO/STO), under tensile strain, and on LAO substrates (NNO/LAO), nearly strain-free. In the latter, the scaling of $\rho(T)$ is independent of the T_a and gives rise to $n = 1$[37], as in the bulk material[27,28] and in agreement with ref. [30]. We believe this is attributed to a low V_o content compared with the other two systems, which is supported by values of ρ that are one order of magnitude lower in the metallic state of NNO/LAO film compared with that of the NNO/STO and NNO/YAO films under strain. In the case of tensile strained films (NNO/STO), strain and defect formation are correlated since defects are created during growth as a mechanism to enlarge the lattice and achieve epitaxy[37]. In the current case of compressively strained NNO/YAO, there is no natural tendency for the film to favor vacancies, so these can be created and removed purposely, and the effects of strain and oxygen content can be separated, as shown in Fig. 2b.

The validity of the $n = 1$ exponent from above the $T_{MI} = 170$ K (and even from $T_{MI} = 100$ K in NNO/LAO), significantly smaller than the Debye temperature of the material (420 K[27,30]), casts questions about its origin being on electron-phonon interactions and points to the strange metal behavior of $NdNiO_3$. Strange metal behavior is characterized by Planckian dissipation, whose origin is still under debate[25], that supports a resistivity that scales linearly with temperature and is independent of the nature of the electron interactions. Recent theoretical calculations have shown that Planckian metal behavior can also originate from a disordered Hubbard model (with electron interactions that do not conserve
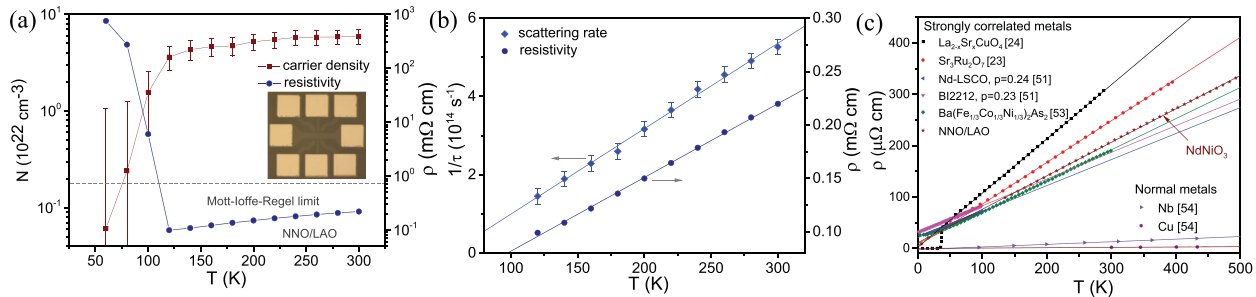
Fig. 5 Strange metal-like T-linear resistivity. a Log of carrier density and log of resistivity of a 5 nm NNO/LAO film as a function of temperature. The inset shows the Hall bar used, with channel dimensions $620 \times 100\ \mu m^2$. The dashed line indicates the Mott–Ioffe–Regel limit in nickelates[22,29]. **b** $1/\tau$ as a function of temperature is plotted together with the resistivity and their linear fits. **c** The T-linear resistivities of reported Planckian metals[23,24,51,53,54] together with that of the NNO/LAO film. In **a** and **b**, error bars indicate the statistical error.

momentum), from which a two-fluid model emerges that consists of localized Sachdev–Ye–Kitaev (SYK) islands interacting with itinerant fermions[12,38,49]. Our results seem consistent with this scenario.

To explicate the underlying physics behind this strange linear-T-resistivity, we use a NNO film grown under low strain conditions on LAO substrate to reduce the defect content to the minimum. Cross-sectional high-angle annular dark-field scanning transmission electron microscopy (HAAFAF-STEM) characterizations reported in our previous work[37] indicate perfectly epitaxial growth with atomically flat interfaces and a pure phase of this film. Commonly reported lattice imperfections in nickelates, such as dislocations and Ruddlesden–Popper faults, are not observed. The low concentration of the lattice defects present is also supported by the ultra-low residual resistivity (e.g., $8.6 \pm 0.22\ \mu\Omega$ cm in the 5 nm film), as shown in Supplementary Fig. 9. Moreover, the ρ values of the NNO/LAO films are well below the Mott–Ioffe–Regel limit[22,29] and display a robust linear-T dependence (from 120 to 500 K). All these features make it an ideal candidate to study the intrinsic origin of the linear-T-resistivity in this material.

Hall measurements shown in Fig. 5a display a nearly constant value (within error bars) of the carrier density (N) in the metallic state, with the expected sharp decrease at and below T_{MI}. We note that the measured N values are larger than those expected from 1 e per Ni atom. This discrepancy could be due to the existence of both electron-like and hole-like states at the E_F[22] or to strong polaronic effects in the metallic state[50], which make reliable measurements of carrier density challenging in nickelates[2].

$1/\tau$ values obtained from these measurements, using Drude's formula $\rho = m^*/Ne^2\tau$ and the reported $m^* = 7m_o$[22], show linear behavior (see Fig. 5b) and nearly follows the universal dissipation law, $1/\tau = akBT/\hbar$, with a constant $a = 9.3 \pm 4.0$, larger than that expected in Planckian metals[23,26,51,52]. However, if a more physically meaningful value of the carrier density is used ($N = 1.0 \times 10^{22} cm^{-3}$[22,50]), a value of $a = 1.8 \pm 0.4$, in the proximity of the Planckian dissipation bound ($a = 1$) is obtained. Indeed, the behavior of $NdNiO_3$ is comparable to that of other reported Planckian metals, in the same temperature range, as shown in Fig. 5c, as well as in Supplementary Table 1[23,24,51,53,54]. Our observations, therefore, suggest that further work is required to fully understand the metallicity of this materials family.

To conclude, in oxygen-deficient $NdNiO_3$, metallic regions coexisting with semiconducting defective regions, undergo local metal-insulator transitions, visible above the percolation threshold as thermal hysteresis in the resistivity. Only by further increasing the volume fraction of the pristine state, the metal-insulator transition is unveiled as a change in the slope sign of the resistivity. The $n = 1$ exponent of ρ-T is recovered upon sufficient oxygenation. This establishes the intrinsic T-linear resistivity in metallic $NdNiO_3$ and postulates its strange metal behavior.

Although reliable quantification of the carrier density and the value of a in nickelates remains challenging, these results provide experimental support for the disorder-induced two-fluid origin of Planckian dissipation.

METHODS

Synthesis of oxygen-deficient $NdNiO_{3-\delta}$ film

An epitaxial NNO film with thickness of 20 nm was deposited on a single-crystal $YAlO_3$ substrate by pulsed laser ablation of a single-phase target (Toshima Manufacturing Co., Ltd.). Before deposition, the YAO substrates were thermally annealed at 1050 °C in a flow of O_2 and etched with DI water to obtain an atomically flat surface with single terminated terraces. The growth was performed at 700 °C with an oxygen pressure of 0.2 mbar. The laser fluence on the target was 2 J/cm². After deposition, the samples were cooled down to room temperature under high vacuum ($\leq 10^{-7}$ mbar) to produce an initial $NdNiO_{3-\delta}$ state with a large oxygen vacancy content. The thicknesses, crystal orientation and phase purity of the films were assessed using X-ray diffraction by means of 2θ -ω scans on a Panalytical, Xpert MRD Pro diffractometer.

Control of V_o content in film

The oxygen content in the $NdNiO_{3-\delta}$ film was tuned by annealing in an oxygen-enriched environment (400 cc/min) with a step-by-step increased temperature. In this annealing process, the V_o in the lattice were gradually refilled with the oxygen atoms from the atmosphere. The content of V_o in the lattice can then decreased gradually by increasing the annealing temperature or annealing time.

Electrical properties measurement

The electrical transport properties of the film at each stage of annealing were measured between 5 K and 400 K by the van der Pauw method in a Quantum Design Physical Property Measurement System (PPMS), using a Keithley 237 current source and a Agilent 3458A multimeter. For Hall measurement, the films were patterned into Hall bar (channel dimensions $620 \times 100\ \mu m^2$) using photolithography and ion etching. The Pt electrodes with a thickness of 80 nm were fabricated using e-beam evaporation to provide an ohmic contact with the film.

Conduction maps

For the conductive-AFM measurements, the $NdNiO_3$ film (on top of an insulating substrate) was connected to a bottom metallic plate on the sides of the substrate by silver paste. The bottom plate was connected to the ground of the AFM microscope and a DC bias voltage was applied between the tip and sample. The measurement was performed using a TUNA™ amplifier (Bruker Corp.) with Pt/Ir coated silcon tip.

DATA AVAILABILITY

REFERENCES

1. Canfield, P., Thompson, J., Cheong, S. W. & Rupp, L. Extraordinary pressure dependence of the metal-to-insulator transition in the charge-transfer compounds NdNiO$_3$ and PrNiO$_3$. *Phys. Rev. B* **47**, 12357–12360 (1993).
2. Catalano, S. et al. Rare-earth nickelates RNiO$_3$: thin films and heterostructures. *Rep. Prog. Phys.* **81**, 046501 (2018).
3. Amboage, M., Hanfland, M., Alonso, J. & Martinez-Lope, M. High pressure structural study of SmNiO$_3$. *J. Phys. Conden. Matt.* **17**, S783–S788 (2005).
4. Shi, J., Ha, S. D., Zhou, Y., Schoofs, F. & Ramanathan, S. A correlated nickelate synaptic transistor. *Nat. Commun.* **4**, 2676 (2013).
5. Ha, S. D., Vetter, U., Shi, J. & Ramanathan, S. Electrostatic gating of metallic and insulating phases in SmNiO$_3$ ultrathin films. *Appl. Phys. Lett.* **102**, 183102 (2013).
6. Bubel, S. et al. The electrochemical impact on electrostatic modulation of the metal-insulator transition in nickelates. *Appl. Phys. Lett.* **106**, 122102 (2015).
7. Ojha, S. K. et al. Anomalous electron transport in epitaxial NdNiO$_3$ films. *Phys. Rev. B* **99**, 235153 (2019).
8. Domínguez, C. et al. Length scales of interfacial coupling between metal and insulator phases in oxides. *Nat. Mater.* **19**, 1182–1187 (2020).
9. Mattoni, G. et al. Striped nanoscale phase separation at the metal-insulator transition of heteroepitaxial nickelates. *Nat. Commun.* **7**, 13141 (2016).
10. Preziosi, D. et al. Direct mapping of phase separation across the metal-insulator transition of NdNiO$_3$. *Nano Lett.* **18**, 2226–2232 (2018).
11. Post, K. et al. Coexisting first-and second-order electronic phase transitions in a correlated oxide. *Nat. Phys.* **14**, 1056–1061 (2018).
12. Li, J. et al. Scale-invariant magnetic textures in the strongly correlated oxide NdNiO$_3$. *Nat. Commun.* **10**, 4568 (2019).
13. Lee, J. H. et al. Imaging and harnessing percolation at the metal-insulator transition of NdNiO$_3$ nanogaps. *Nano Lett.* **19**, 7801–7805 (2019).
14. Li, D. et al. Superconductivity in an infinite-layer nickelate. *Nature* **572**, 624–627 (2019).
15. Osada, M. et al. A superconducting praseodymium nickelate with infinite layer structure. *Nano Lett.* **20**, 5735–5740 (2020).
16. Wang, L. et al. Oxygen vacancy induced room-temperature metal-insulator transition in nickelate films and its potential application in photovoltaics. *ACS Appl. Mater. Interfaces* **8**, 9769–9776 (2016).
17. Heo, S., Oh, C., Son, J. & Jang, H. M. Influence of tensile-strain-induced oxygen deficiency on metal-insulator transitions in NdNiO$_{3-\delta}$ epitaxial thin films. *Sci. Rep.* **7**, 4681 (2017).
18. Onozuka, T. et al. Reversible changes in resistance of perovskite nickelate NdNiO$_3$ thin films induced by fluorine substitution. *ACS Appl. Mater. Interfaces* **9**, 10882–10887 (2017).
19. Kotiuga, M. et al. Carrier localization in perovskite nickelates from oxygen vacancies. *Proc. Natl Acad. Sci. USA* **116**, 21992–21997 (2019).
20. Zhang, Y. et al. Flexible metal-insulator transitions based on van der Waals oxide heterostructures. *ACS Appl. Mater. Interfaces* **11**, 8284–8290 (2019).
21. Harisankar, S., Soni, K., Yadav, E. & Mavani, K. R. Strain-mediated effects of oxygen deficiency and variation in non-Fermi liquid behavior of epitaxial PrNiO$_{3-\delta}$ thin films. *J. Phys. Condens. Mat.* **31**, 135601 (2019).
22. Jaramillo, R., Ha, S. D., Silevitch, D. & Ramanathan, S. Origins of bad-metal conductivity and the insulator-metal transition in the rare-earth nickelates. *Nat. Phys.* **10**, 304–307 (2014).
23. Bruin, J., Sakai, H., Perry, R. & Mackenzie, A. Similarity of scattering rates in metals showing T-linear resistivity. *Science* **339**, 804–807 (2013).
24. Giraldo-Gallo, P. et al. Scale-invariant magnetoresistance in a cuprate superconductor. *Science* **361**, 479–481 (2018).
25. Patel, A. A. & Sachdev, S. Theory of a Planckian metal. *Phys. Rev. Lett.* **123**, 066601 (2019).
26. Zaanen, J. et al. Planckian dissipation, minimal viscosity and the transport in cuprate strange metals. *SciPost Phys.* **6**, 061 (2019).
27. Rajeev, K., Shivashankar, G. & Raychaudhuri, A. Low-temperature electronic properties of anormal conducting perovskite oxide (LaNiO$_3$). *Solid State Commun.* **79**, 591–595 (1991).
28. Blasco, J., Castro, M. & Garcia, J. Structural, electronic, magnetic and calorimetric study of the metal-insulator transition in NdNiO$_{3-\delta}$. *J. Phys. Condens. Mat.* **6**, 5875–5889 (1994).
29. Mikheev, E. et al. Tuning bad metal and non-Fermi liquid behavior in a Mott material: Rareearth nickelate thin films. *Sci. Adv.* **1**, e1500797 (2015).
30. Liu, J. et al. Heterointerface engineered electronic and magnetic phases of NdNiO$_3$ thin films. *Nat. Commun.* **4**, 2714 (2013).
31. Kobayashi, H. et al. Pressure-induced unusual metallic state in EuNiO$_3$. *Phys. Rev. B* **91**, 195148 (2015).
32. Yadav, E., Harisankar, S., Soni, K. & Mavani, K. Influence of Cu doping and thickness on non-Fermi liquid behaviour and metallic conductance in epitaxial PrNiO$_3$ thin films. *Appl. Phys. A* **124**, 614 (2018).
33. Phanindra, V. E., Agarwal, P. & Rana, D. Terahertz spectroscopic evidence of non-Fermi liquid-like behavior in structurally modulated PrNiO$_3$ thin films. *Phys. Rev. Mater.* **2**, 015001 (2018).
34. Stemmer, S. & Allen, S. J. Non-Fermi liquids in oxide heterostructures. *Rep. Prog. Phys.* **81**, 062502 (2018).
35. Herranz, G. et al. Effect of disorder on the temperature dependence of the resistivity of SrRuO$_3$. *Phys. Rev. B* **77**, 165114 (2008).
36. Patel, N. D., Mukherjee, A., Kaushal, N., Moreo, A. & Dagotto, E. Non-Fermi liquid behavior and continuously tunable resistivity exponents in the Anderson-Hubbard model at finite temperature. *Phys. Rev. Lett.* **119**, 086601 (2017).
37. Guo, Q., Farokhipoor, S., Magén, C., Rivadulla, F. & Noheda, B. Tunable resistivity exponents in the metallic phase of epitaxial nickelates. *Nat. Commun.* **11**, 2949 (2020).
38. Lee, K., Patel, A., Trivedi, N. & Sachdev, S. Emergent interacting two-fluids in a disordered Hubbard model. *APS* **2019**, H06–005 (2019).
39. Mott, N. F. Conduction in non-crystalline materials: III. Localized states in a pseudogap and near extremities of conduction and valence bands. *Philos. Mag.* **19**, 835–852 (1969).
40. Shlimak, I. *Is hopping a science? Selected topics of hopping conductivity* (World Scientific, 2015).
41. Bergman, D. J. & Stroud, D. Physical properties of macroscopically inhomogeneous media. *Solid State Phys.* **46**, 147–269 (1992).
42. Kumar, S. & Majumdar, P. Singular effect of disorder on electronic transport in strongly coupled electron-phonon systems. *Phys. Rev. Lett.* **94**, 136601 (2005).
43. Xiang, P.-H. et al. Strain controlled metal-insulator transition in epitaxial NdNiO$_3$ thin films. *J. Appl. Phys.* **114**, 243713 (2013).
44. Catalan, G., Bowman, R. & Gregg, J. Metal-insulator transitions in NdNiO$_3$ thin films. *Phys. Rev. B* **62**, 7892–7900 (2000).
45. Medarde, M. L. Structural, magnetic and electronic properties of RNiO$_3$ perovskites (R = rare earth). *J. Phys. Condens. Mat.* **9**, 1679–1707 (1997).
46. Laffez, P., Zaghrioui, M., Monot, I., Brousse, T. & Lacorre, P. Microstructure and metalinsulator transition of NdNiO$_3$ thin films on various substrates. *Thin Solid Films* **354**, 50–54 (1999).
47. Granados, X., Fontcuberta, J., Obradors, X. & Torrance, J. Metastable metallic state and hysteresis below the metal-insulator transition in PrNiO$_3$. *Phys. Rev. B* **46**, 15683–15688 (1992).
48. Liu, S. et al. Random field driven spatial complexity at the Mott transition in VO$_2$. *Phys. Rev. Lett.* **116**, 036401 (2016).
49. Lee, K., Patel, A., Trivedi, N. & Sachdev, S. Microscopic origin of the 'strange' metal. *Bull. Am. Phys. Soc.* **65**, 1 (2020).
50. Ha, S. D. et al. Hall effect measurements on epitaxial SmNiO$_3$ thin films and implications for antiferromagnetism. *Phys. Rev. B* **87**, 125150 (2013).
51. Legros, A. et al. Universal T-linear resistivity and Planckian dissipation in overdoped cuprates. *Nat. Phys.* **15**, 142–147 (2019).
52. Cao, Y. et al. Strange metal in magic-angle graphene with near Planckian dissipation. *Phys. Rev. Lett.* **124**, 076801 (2020).
53. Nakajima, Y. et al. Quantum-critical scale invariance in a transition metal alloy. *Commun. Phys.* **3**, 181 (2020).
54. Gunnarsson, O., Calandra, M. & Han, J. Colloquium: Saturation of electrical resistivity. *Rev. Mod. Phys.* **75**, 1085–1099 (2003).

AUTHOR CONTRIBUTIONS
Q.G. and B.N. designed the experiments. Q.G. grew and characterized the NNO films and analyzed the structural and transport data under the supervision of B.N. Q.G. and B.N. wrote the paper.

COMPETING INTERESTS
The authors declare no competing interests.

ADDITIONAL INFORMATION

Publisher's note Springer Nature remains neutral with regard to jurisdictional claims in published maps and institutional affiliations.